

# Computational Investigation of Carbon Based Anode Materials for Li- and Post-Li- Ion Batteries

Jafar Azizi,<sup>[a]</sup> Axel Groß,<sup>[a, b]</sup> and Holger Euchner<sup>\*[c]</sup>

Due to its negligible capacity with respect to sodium intercalation, graphite is not suited as anode material for sodium ion batteries. Hard carbon materials, on the other hand, provide reasonably high capacities at low insertion potential, making them a promising anode materials for sodium (and potassium) ion batteries. The particular nanostructure of these functionalized carbon-based materials has been found to be crucially linked to the material performance. However, there is still a lack of understanding with respect to the functional role of structural units, such as defects, for intercalation and storage.

To overcome these problems, the intercalation of Li, Na, and K in graphitic model structures with distinct defect configurations has been investigated by density functional theory. The calculations confirm that defects are able to stabilize intercalation of larger alkali metal contents. At the same time, it is shown that a combination of phonon and band structure calculations are able to explain characteristic Raman features typically observed for alkali metal intercalation in hard carbon, furthermore allowing for the quantification of the alkali metal intercalation inbetween the layers of hard carbon anodes.

## Introduction

Lithium-ion batteries (LIBs) are essential for storing electrical energy, extending from portable electronic devices to e-mobility.<sup>[1–4]</sup> Due to the foreseeable scarcity of lithium, however, alternative solutions based on more abundant materials have become the subject of contemporary research and investigation. Here, sodium-<sup>[5]</sup> and potassium-ion batteries<sup>[6]</sup> (SIBs and KIBs), frequently categorized as post-Li-ion batteries, are the most appealing candidates at the moment. Generally, it has to be pointed out that, with respect to their potential as drop-in replacements for LIBs, there are significant differences in the physicochemical properties of sodium and potassium as compared to lithium. These range from different coordination preferences in compounds to largely varying desolvation energies.<sup>[7,8]</sup> Hence, finding suitable electrode materials for post-Li-ion batteries and understanding their physical and chemical properties is of utmost importance to advance these technologies.

Graphite based materials are still the anode of choice for Li-ion batteries. However, while the lithiation process of graphite results in a succession of binary graphite intercalation com-

pounds (GICs) with a theoretically maximum capacity of 372 mA<sub>h</sub>g<sup>-1</sup> for the final LiC<sub>6</sub> stoichiometry, no binary intercalation compounds of graphite with significant sodium content do exist, and hence graphite shows only negligible sodium storage capacity.<sup>[9]</sup> It has to be noted that this is not simply originating from the larger ionic radius of Na as the even larger K ions have been shown to form GICs.<sup>[10–15]</sup> In fact, according to theoretical results across all alkali metals (AM), sodium has the weakest chemical binding to a given substrate, indicating that this variation in behavior is not unique to graphite.<sup>[16]</sup>

Consequently, different alternative anode materials have to be considered for NIBs, resulting in hard carbons as promising candidates in particular for Na- and K-ion batteries. The structure of HC is typically described as being composed of differently sized micro- and nano-pores framed by randomly oriented, often curved graphitic domains with large defect concentrations and increased interlayer spacing.<sup>[17–20]</sup> Carbon atoms within a graphitic layer (of such a domain) are linked by strong covalent bonds, while van der Waals forces are responsible for the interaction between neighbouring layers. Topological defects, which result in the presence of non-hexagonal arrangements of carbon atoms in the graphitic layers, play a crucial role for the diverse morphology and characteristic properties of HCs, as e.g. curved geometries may be explained by their presence.<sup>[21]</sup> Unlike graphite, which has a d-spacing of 335 pm, the inter-layer spacing of HCs is enhanced and can amount to more than 400 pm which has been proposed to facilitate ion insertion. Especially, synthesis temperature and raw material composition have significant impact on the electrochemical performance of HCs, resulting in a large variation of experimentally observed capacities. For Li-insertion in HC reversible capacities ranging from 210 to 675 mA<sub>h</sub>g<sup>-1</sup><sup>[22,23]</sup> are reported, while in case of Na and K, values from 260 to 640 mA<sub>h</sub>g<sup>-1</sup><sup>[24]</sup> and 250 to 336 mA<sub>h</sub>g<sup>-1</sup><sup>[25–27]</sup> have been observed. For instance, when phenolic resin-derived HC is prepared at different temperatures, 1100 °C, 1300 °C, and

[a] J. Azizi, A. Groß  
Institute of Theoretical Chemistry, Ulm University, D-89081 Ulm

[b] A. Groß  
Helmholtz Institute Ulm for Electrochemical Energy Storage, D-89081 Ulm

[c] H. Euchner  
Institute of Physical and Theoretical Chemistry, University of Tübingen,  
72076 Tübingen, Germany  
E-mail: holger.euchner@uni-tuebingen.de

Supporting information for this article is available on the WWW under <https://doi.org/10.1002/cssc.202301493>

© 2024 The Authors. ChemSusChem published by Wiley-VCH GmbH. This is an open access article under the terms of the Creative Commons Attribution License, which permits use, distribution and reproduction in any medium, provided the original work is properly cited.

1500 °C, the initial reversible capacities for Na intercalation are 337, 358, and 386 mAhg<sup>-1</sup>, with initial Coulombic efficiencies of 82%, 81%, and 85%, respectively. Similar scenario have been observed for Li and K as well.<sup>[28]</sup>

With respect to the insertion mechanism and structure of the HC, the largely accepted card house model (and modifications thereof) allows for a qualitative description of the processes that underly the observed voltage profile in a charge-discharge curve.<sup>[29–36]</sup> The currently accepted modification of this model assumes that alkali metal atoms are initially adsorbed on surface and defect sites, followed by the insertion between the layers of graphitic domains in the later part of the sloping potential region of the charge-discharge curve, whereas the flat low potential region corresponds to the adsorption in micro- and nano-pores, with the potential actually being close to that one of metal deposition.<sup>[31–39]</sup>

For the characterization of graphitic materials, often Raman scattering is applied.<sup>[31]</sup> The main Raman peak that is typically observed is the so-called G-band, which normally appears at about 1580 cm<sup>-1</sup> and is related to the in-plane motion of the carbon atoms in the graphitic planes. Interestingly, the presence of defects results in the additional observation of the so-called D-band at around 1360 cm<sup>-1</sup>. However, the D-band does not correspond to a  $\Gamma$ -point phonon, as is the case for normal Raman modes. Instead, it results from a more intricate inter-valley phenomenon known as double resonance and contains indirect information on the electronic band structure.<sup>[40,41]</sup>

For a knowledge based design of hard carbon anodes, the impact of structural factors such as porosity, carbon binding motifs, and even heteroatom concentration on the functionality of the material must be understood.<sup>[42–44]</sup> While there have been several theoretical studies regarding the role of defects in graphitic systems, defect types, and their functionality have not been thoroughly considered in these investigations.<sup>[45–47]</sup> Therefore, by investigating the impact of defects on the alkali metal storage mechanisms, we have made a first step towards such an understanding. In this work, the impact of different types of carbon defects on intercalation sites and voltages, vibrational properties and electronic band structure was studied with respect to the intercalation of Li, Na and K. Defects are known to be abundant in HC<sup>[17–20]</sup> and strongly interact with metal atoms. Hence the fraction of atoms that can be intercalated, especially in the case of Na, increases significantly in the presence of defects. Thus, due to their significant impact, considering the intercalation/adsorption processes at defect sites is necessary for properly describing the AM storage mechanism. While defects obviously do affect the local atomic configuration, it will be demonstrated that the basic features of the band structure and the phonon dispersion curves remain unaffected.

Finally, it has to be pointed out that the presence of defects will also be important for the formation of the solid-electrolyte interface (SEI). During operation in an electrochemical environment a SEI is formed on hard carbon anodes, which is known to depend on the utilized electrolyte and typically consists of inorganic oxides, fluorides and carbonates (inner layer) as well

as organic products (outer layer). The functioning of the SEI is to prevent further reduction of the electrolyte by offering chemical stability combined with good ionic transport properties. While the growth of the SEI on HC anodes is certainly also influenced by the HC morphology, the focus of this work lies on the AM intercalation in the electrode.<sup>[48]</sup>

## Computational Methods

To investigate the impact of different structural motives on the properties of hard carbon, model systems have been studied by density functional theory (DFT). A periodic setup, consisting of a stacking of two graphitic layers was used to describe the bulk structure of hard carbon. Without defects such an arrangement corresponds to bulk graphite (AB stacking), while for the investigation of defects it separates the defect containing layer by one ideal (defect-free) layer, thus avoiding defect-defect interactions. The impact of additional graphitic layers in the supercell was carefully checked, yielding changes in the formation energies in the meV range. For the same reasons, the lateral size of the simulation cell was chosen rather large to correctly represent the investigated defects (see Figure 3).

Different defect types and the resulting intercalation sites have been investigated in supercells of AMC<sub>108-x</sub> and AMC<sub>144-x</sub> stoichiometry. Furthermore, to mimic the Li, Na, and K intercalation process, defect containing GIC model structures with increasing AM content – derived from supercells with AMC<sub>6r</sub>, AMC<sub>8r</sub>, AMC<sub>12r</sub>, AMC<sub>24</sub> and AMC<sub>48</sub> stoichiometry – have been investigated. All simulations were performed with the Vienna Ab Initio Simulation Package (VASP),<sup>[49]</sup> using the Projector Augmented Wave (PAW) approach.<sup>[50]</sup> Exchange and correlation were described via the optPBE functional, which includes a non-local correction scheme to account for van der Waals interactions.<sup>[51]</sup> The optPBE functional was chosen, as this functional has been shown earlier to yield accurate results for describing graphite and the intercalation of AMs therein.<sup>[52]</sup> Each structure, was optimized with respect to lattice constant and atomic positions, applying a plane wave cutoff of 600 eV. The structures based on the C<sub>108</sub> supercell was computed with a 4×4×4 k-point mesh, while the other system sizes under investigation were optimized with similar k-point resolution. For the determination of the electronic band structure the number of k-points was doubled. The phonopy code and the finite displacement method were used to determine the vibrational properties.<sup>[53]</sup> Finally, the resulting phonon dispersion curves and electronic band structures were back-folded to the first BZ of graphite, allowing for a direct comparison along the high-symmetry directions  $\Gamma$  ( $\Gamma - K - M - \Gamma$ ). For the backfolding of the phonon dispersion curves the Phonon Unfolding code has been used, whereas the bandup code has been applied for the backfolding of the electronic band structure.<sup>[54–56]</sup>

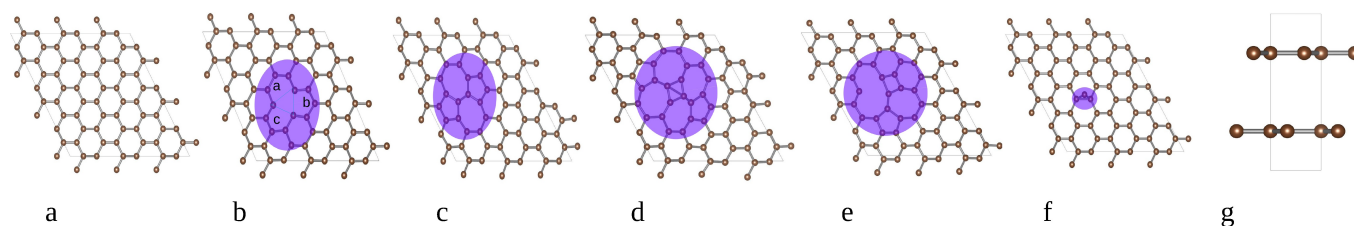


**Figure 1.** Different kinds of defects present in graphite. (a) pristine graphite (b) mono-vacancy (MV) (c) Stone-wales defect (SW) (d) double rotation (DR) (e) mono-vacancy + Stone-wales (MSW) (f) add atom (AA) and (g) side view of the structure used for defect creation.

## Results and Discussion

### Defect Structure

To gain a basic understanding of the morphology and storage mechanism in hard carbon, the impact of different defect motives on the alkali metal insertion has been investigated. For this purpose, defect motives comprising mono-vacancy (MV), Stone-Wales defect (SW), double rotation (DR), add atom (AA), and a combination of monovacancy and Stone-Wales defect (MSW) have been introduced in the simulation cell. Figure 1 depicts the defect containing layer of the two layer simulation cell as well as a defect-free graphite sheet for comparison.

The most simple defects in graphitic materials are monovacancies, which are obtained by the removal of a carbon atom. This results in three undercoordinated carbon atoms that are triangularly arranged (see Figure 1b)) and typically bend out of the graphitic plane. The Stone-Wales (SW) defect is considered to be one of the most important topological defects in graphitic materials. It is created by turning four hexagons into two heptagons and two pentagons, which is achieved by the so-called SW transformation, the rotation of one C–C bond by an angle of 90°, as depicted in Figure 1c). Furthermore, our model configurations also contain a double rotation (DR) which consists in the transformation of eight hexagons into four heptagons, two pentagons and one tetragon as a result of a 90° rotation of two neighboring C–C bonds. This defect usually causes the bending of the graphene sheets, perpendicular to the line that connects the two pentagons (see Figure 1d)). Moreover, the combination of a MV and SW defect has been constructed (see Figure 1e)). Joining the structural motifs of these two defects yields a new defect type, consisting of a tetragon, a pentagon, a heptagon, and a decagon. Finally, a carbon adatom placed close to one of the graphitic layers was investigated, and has been found to preferentially adsorb on a bridge site, while adsorption in the center of a hexagon and directly on top of a carbon atom is less favorable. The carbon adatoms thus results in a triangular configuration on top of the graphitic plane, showing a slightly increased C–C bond length of 1.55 Å as compared to the in plane bond length of 1.5 Å.

Interestingly, the introduction of the defects in our model system has been found to result in a stabilization of the AB stacking, such that for the cases of SW, MSW and MV even an AA-stacked starting configuration is not preserved. The defect containing systems transform to an AB stacking, whereas a defect-free system retains the meta-stable AA-stacking. Finally,

it has to be noted that the defects result in slight changes in the C–C bond lengths, however, the effect decreases with increasing distance from the defect center. In the case of the adatom, the layers also prefer to be shifted against each other, however, not a full AB stacking is reached. Instead the layers shift such that the adatom is in the center of a hexagon in one layer, while it is covalently bound to two carbon atoms in the other (on top of a C–C bond).

### Energetic Stability

The probability of finding a certain defect, is largely determined by the energetic penalty going along with the defect formation. Therefore, we have calculated the defect formation energies for the above introduced defect types (see Figure 2). A defect's formation energy is defined as

$$E_f = E_d - E_p + \mu n \quad (1)$$

where  $E_d$  and  $E_p$  are the total energy of the defective and defect-free system, respectively.  $\mu$  is the chemical potential of carbon, which is estimated by the total energy per atom in graphite, multiplied by the number of removed atoms  $n$ .

The resulting formation energies for MV, SW and AA defect amount to 6.9, 4.0 and 6.2 eV, which is in reasonable agreement with literature (7.3–7.5, 4.5–5.3, and 6.3–8.5 eV for MV, SW and AA respectively).<sup>[52,57,58]</sup> The fact that the here obtained values

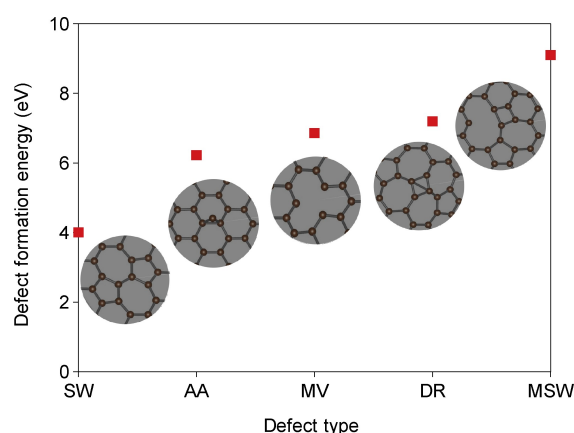


**Figure 2.** Formation energy for the different kinds of defects present in graphite, Stone Wales defect (SW), adatom (AA), mono-vacancy (MV), double rotation (DR) and MSW.

are slightly lower is likely to be a consequence of different exchange-correlation functionals. While the obtained formation energies clearly show that the SW defect is the most stable of the investigated defect types, the AA is found to be more stable than the MV and the DR (see Figure 2). Finally, the MSW defect is found to be almost 1.8 eV more stable than the sum of a SW and a MV defect, thus pointing to the reciprocal affinity of defects.<sup>[59]</sup> This is well known for the case of graphite where defect clusters develop during the early stages of melting at elevated temperatures.

### Single Atom Intercalation

Despite the rather high costs for defect formation, precursors and preparation conditions of hard carbon at temperatures

typically above 1200 K result in large defect concentrations. Moreover, it has to be noted that defects are often suggested to be one of the reason for the rumpled texture of graphite that is sometimes observed experimentally.<sup>[60]</sup> To elucidate the impact of defects with respect to the use of carbon derivatives as anode material, we have investigated the most favorable intercalation sites for Li, Na, and K in the presence of the simplest defects – MV, SW and AA defect as well as for the case of a MSW defect – and compare it to the intercalation in the defect-free case. For these systems, the energetic stability of a single alkali metal atom at different characteristic positions of the defect structures (see Figure 3) was investigated by calculating the intercalation energy with respect to the AM-free system:

$$E_{int} = E_{def+AM} - (E_{def} + E_{AM}) \quad (2)$$

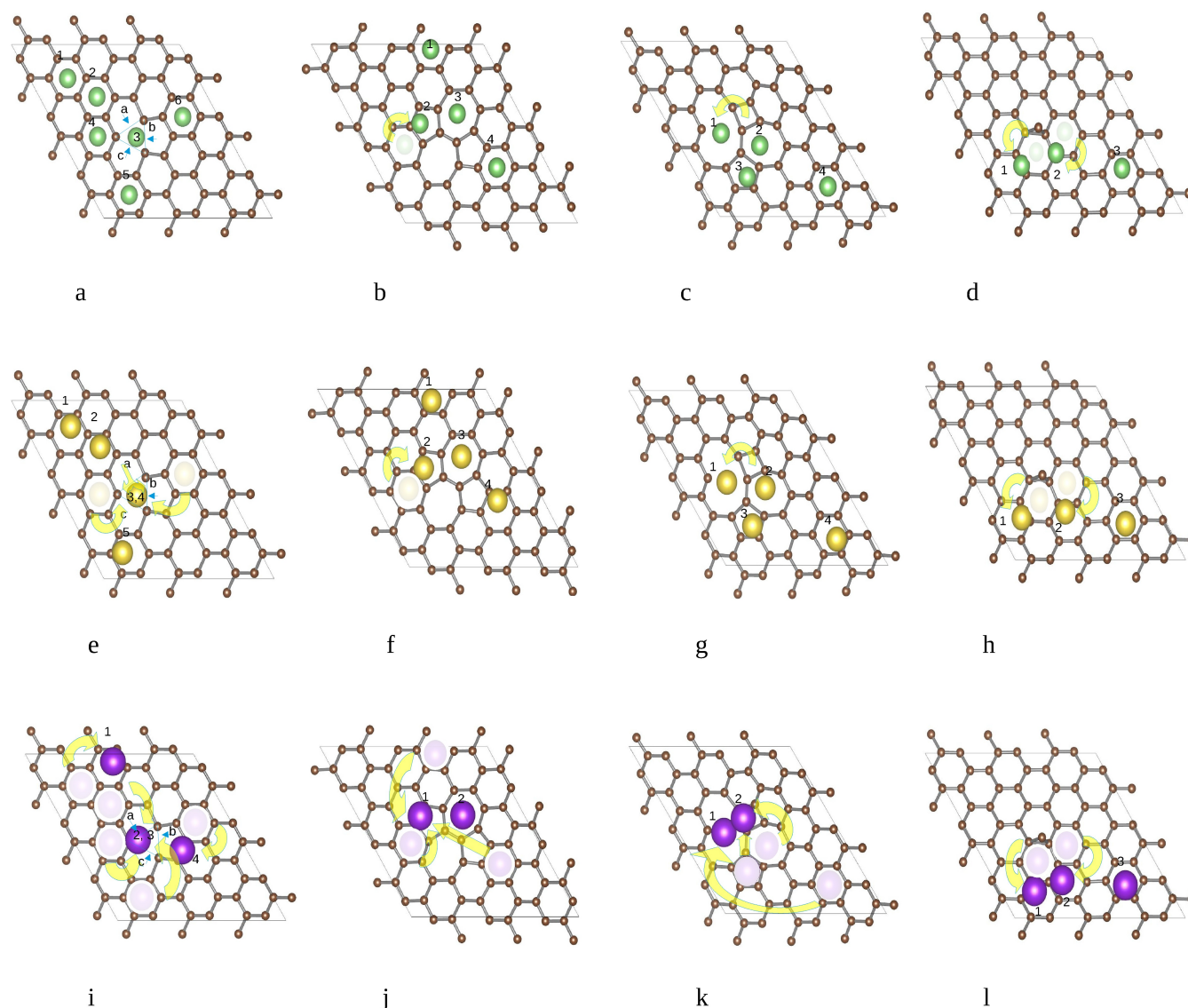


**Figure 3.** Schematic representation of possible Li- (top), Na- (middle) and K- (bottom) intercalation sites for the different two-layer model systems a),e),i) MV defect b),f),j) SW defect c),g),k) MSW d),h),l) AA defect. Atoms that have moved to a neighboring site are shown in faint color with an arrow indicating the site they have moved to. COMMENT: UNFORTUNATELY THE FIGURE IS STILL CORRUPTED. I IS BETTER BUT SOME NUMBERS ARE STILL MISSING AND SOME LAYERS SHIFTED



Here,  $E_{def+AM}$  is the total energy of the graphitic (defect containing) system after the insertion of one AM atom, and  $E_{def}$  is the energy of the AM-free layers, whereas  $E_{AM}$  is the energy of the AM in the bulk metal phase.

First, the intercalation of an AM atom in defect-free AA and AB type layers with enforced stacking sequence was investigated for the  $C_{108}$  supercell. While the AB stacking (i.e. pristine graphite) is more stable for the AM-free system (by about  $\approx 7$  meV/at), the intercalation of one AM atom – corresponding to an  $AMC_{108}$  stoichiometry – does result in different scenarios. The intercalation of one Li atom is energetically favorable (see Table 1), with the AB stacking remaining the more stable configuration. Li is sitting above the center of a hexagon in one layer, while being on top of a carbon atom for the other. However, already by intercalating one Li atom, the difference in energy between the AA and the AB stacking is reduced to  $\approx 4$  meV/at. This indicates that further Li intercalation can be expected to result in a stabilization of the AA stacking. For the intercalation of one Na atom, the most stable configuration also corresponds to an AB stacking, however, the Na intercalation is indeed energetically unfavorable, as can be inferred from the positive insertion energy in Table 1. While an AA stacking is found to be less stable, an intermediate stacking involving both AA and AB stacking with the energy almost identical to the AB stacked case was also observed. Finally, for the insertion of one K atom, again the AB stacking is found to be energetically most stable, however, the AA stacking (and an intermediate stacking sequence) is found to be energetically almost degenerate (all within 1 meV/at). Yet, surprisingly, the K intercalation is also found to be energetically largely unfavorable (see Table 1). In contrast to the case of Na, the K intercalation, however, becomes energetically favorable at larger K contents as can be inferred from Table 1 for the case of  $AMC_{48}$ . Interestingly, for all cases the AB stacking is preserved for low AM concentrations. The reason is that the van der Waals forces between two adjacent layers prevail over the energy gain obtained by the insertion of a low AM fraction. However, the decreasing energy differences between the different stackings already indicate that for larger AM fractions a transition to an AA stacking with the AMs above and below a carbon hexagon can be expected – as is indeed already observed for the case of  $AM_{48}$  (see Table 1). This alkali metal concentration is just on the verge of favoring an AA stacking. In fact, in the case of Na and K, the AA stacked configuration is already the more stable one, while for Li the AB stacking is still slightly favored. The observed trend towards an

AA stacking corresponds to the sequence of the typical intercalation compounds with increased carbon content, as discussed in literature.<sup>[61]</sup>

Regarding the equivalent situation for the corresponding defect containing systems, clearly shows that the presence of defects can stabilize the insertion of AMs in graphite derivatives, however, the insertion energy strongly depends on the respective intercalation site (see Table 2). Furthermore, as already mentioned above, MV, SW and MSW defects stabilize the AB type stacking, which is then to a large extent also preserved for the low AM contents discussed in the following.

In the case of the MV, the intercalation of a Li atom in one of the three hexagons that get connected by the creation of the MV defect (see Figure 3a)), results in the Li atom moving towards the defect center (position 3), which, as one may have expected, is the energetically most stable site. On the other hand, if a Li atom is placed inside an intact hexagon (position 1, 2, 4, 5 and 6), the atom remains at the center of this site, however, with significantly less energy gain (see Table 2). For Na atoms the situation is similar, however, due to their size an off-center position in the hexagonal sites is more favorable due to the interaction with the second layer. As in the case of Li, the site at the defect center is energetically most stable, yielding negative intercalation energies. Here, it has to be noted that two slightly different positions are observed (position 3 and 4), with the Na atom either moving towards an undercoordinated carbon atom or between two such atoms – i.e. the Na atom moves either to a corner or to a side of the indicated triangle. The observed negative intercalation energy clearly shows the stabilizing effect of the MV defect for Na intercalation as compared to pristine graphite. Thus, close to the MV defect center, the intercalation of Li and Na is strongly favored, while with increasing distance to this site the insertion energy approaches the situation for defect-free graphitic layers.

**Table 1.** Intercalation energy  $E_{int}$  (in eV) for Li, Na and K, regarding AA and AB stacked graphite, for the  $C_{108}$  and  $C_{48}$  model systems. The energy difference between AA and AB stacked graphite corresponds to  $E_{AB} - E_{AA} = -0.79$  and  $-0.35$  eV for  $C_{108}$  and  $C_{48}$ , respectively. COMMENT: NUMBERS SEEM NOT PROPERLY ALIGNED IN THE COLUMNS

Types	Li	Na	K
$C_{48-AA}$	-0.14	0.39	0.17
$C_{48-AB}$	-0.15	0.40	0.15
$C_{108-AA}$	0.23	0.89	1.33
$C_{108-AB}$	-0.23	0.59	1.11

**Table 2.** Intercalation energy  $E_{int}$  (in eV) for Li, Na and K at the different sites indicated in Figure 3, obtained for the  $C_{108-x}$  model system. Note that empty fields (–) indicate that an atom placed at this position moved to a nearby site. The most stable sites are marked in boldface and have been used as starting point for further intercalation (see text). COMMENT: NUMBERS SEEM NOT PROPERLY ALIGNED

Sites	1	2	3	4	5	6
$Li_{mv}$	-0.48	-0.53	<b>-1.45</b>	-0.53	-0.53	-0.53
$Na_{mv}$	0.23	0.18	<b>-0.54</b>	<b>-0.54</b>	0.18	–
$K_{mv}$	0.38	-0.29	<b>-0.33</b>	0.35	–	–
$Li_{sw}$	-0.34	-0.56	<b>-0.59</b>	-0.40	–	–
$Na_{sw}$	0.30	<b>-0.00</b>	<b>-0.00</b>	0.17	–	–
$K_{sw}$	<b>-0.06</b>	-0.00	–	–	–	–
$Li_{msw}$	<b>-1.63</b>	-0.79	-0.66	-0.52	–	–
$Na_{msw}$	<b>-0.79</b>	-0.17	0.08	0.25	–	–
$K_{msw}$	<b>-0.26</b>	-0.19	–	–	–	–
$Li_{aa}$	-1.01	<b>-1.02</b>	-0.51	–	–	–
$Na_{aa}$	-0.45	<b>-0.49</b>	-0.30	–	–	–
$K_{aa}$	-0.29	<b>-0.34</b>	0.03	–	–	–

For the SW defect, Li atoms move to the center of the created heptagon if they are placed inside the latter one (position 3), whereas placing them on a pentagonal site or a neighboring hexagon results in a shift towards the edges of the pentagon (position 2). Li atoms on hexagonal sites far away from the defect remain centered at these sites (position 1 and 4). Here, again the intercalation in the vicinity of the defect (positions 2 and 3) is found to be the energetically most favorable one (see Table 2). Again, for Na the situation is similar, however, the Na intercalation is stable close to the defect (positions 2 and 3), whereas it becomes unfavorable further away. Furthermore, the tendency of the larger Na atoms to shift towards an off-center position remains. The stabilizing impact of the SW defect is found to be smaller than in the case of the MV. This can be attributed to the fact that the graphitic layers do not contain undercoordinated carbon atoms and thus no dangling bonds with unbound electrons that need to be saturated. Instead, in the case of SW defects only the topology is changed, thus having less significant impact on the intercalation process.

The MSW defect is found to result in significant stabilization of Li at the decagonal site (positions 1). The heptagonal and the slightly off-centered pentagonal site (positions 2 and 3) are also found to be more stable than the hexagonal site further away from the defect (position 4). For Na the same trend is observed with the decagonal site being strongly stabilized. For the above discussed scenarios, the layers keep the AB-stacking sequence after the Li/Na intercalation, meaning that one AM is not enough to induce the transition to an AA stacking in case of a defect being present. While the defect containing layers show no curvature (except DR), they get slightly bent when Li or Na is intercalated. Finally, for the adatom case an intercalated Li moves away from the additional C–C bond. Here, the Li then typically sits close to the center of a top layer hexagon, either on a C–C bond or on top of a C atom (positions 1 and 2), also keeping the AB type stacking. The other situation with Li close to the center of a hexagon and below a carbon atom of the top layer is also possible (position 3), however, energetically significantly less favorable. For Na, the situation is slightly changed. The stacking deviates from AB type with the Na atoms therefore showing a different off-centering. Energetically, however, the Na intercalation remains favorable for these scenarios as well.

Due to the large size of K, the intercalation process in the defect containing structures is somewhat different. While the presence of defects in principle favors an AB stacking, the K intercalation goes along with a significant increase of the layer spacing and hence reduces the van der Waals interaction between the layers. The structure tries to compensate this by getting more strongly curved in the vicinity of the K atom. Hence, we observe a competition between the attractive van der Waals interaction between the layers and the K insertion. This competition is also present in the case of Na, yet to a much smaller extent, whereas it can almost be neglected for the case of Li. For the MV defect K atoms that are further away from the defect move to off-center positions (position 1 and 4), such that they are slightly off-centered in both the defect containing

layer and the defect-free layer sandwiching the AM. Interestingly, these sites are energetically unfavorable as in fact expected from the results for K atoms in the defect free system. In the vicinity of the MV defect, the K atom can again occupy the two energetically slightly different sites, either close to the corner or close to the edge of the indicated triangular shape (position 2 and 3). For the SW defect, the K atom in the defect layer prefers either to be close to the heptagon center (position 2) or on top of a C–C bond connecting a pentagon to a hexagon (position 1). In both cases, the K atom, lies only slightly off-centered with respect to a hexagon in the defect-free layer on top. Energetically, both scenarios result in a slight stabilization of the intercalation process as compared to sites far from the defect. Moreover, it is worth noting that a K atom on the heptagonal site, results in a reduced curvature of the layers. For the MSW case the K atom is found on the sides of the decagon shaped defect (positions 1 and 2), close to an undercoordinated carbon atom. Again the K atom prefers a slightly off-centered position with respect to a hexagon center in the adjacent defect-free layer. This results in a stabilization of the intercalation as compared to the defect free case, with position 1 being energetically more favorable. Finally, the K intercalation in the vicinity of the adatom results in the K atom moving away from the C–C bond. This clearly indicates the impact of the size of the AM atoms. Energetically, positions 1 and 2 become more favorable, whereas an intercalation on position 3 is observed to result in a positive intercalation energy.

In addition, the AM insertion in the larger,  $C_{144}$  based, supercells was investigated. The resulting insertion energies showed qualitatively the same trends as for the  $C_{108}$  based calculations. In particular, the most stable sites were typically found to differ only slightly in position and energy, which can be understood as a consequence of the small differences in AM and defect concentration (see Table S1 in the SI).

To summarize, the comparison with the defect-free system Table 1 makes it clear that only defects are able to stabilize the intercalation of Na and K in the  $C_{108}$  based system, whereas Li can stably be intercalated in AB stacked defect-free graphite. It has to be pointed out that neither Na nor K can stably be intercalated at low concentrations when no defects are present. This is at first glance surprising as K is known to form K-GICs up to at least  $KC_8$  stoichiometry. This can, however, again be understood as consequence of the competition between interlayer van der Waals interactions and the AM–C bonds. Therefore, K intercalation is only stable at higher K concentrations within one layer, since then the gain in energy due to the K–C bonds overcomes the energy penalty of reducing the van der Waals interaction due to an increased layer spacing. This is also the reason why Li-GICs and K-GICs follow different intercalation schemes for dilute AM concentrations.<sup>[6]</sup> For Na the situation is in principle similar to that one of K, however there the intercalation is also unstable at higher Na contents.

On the other hand, this actually indicates that defects may reduce the overpotential needed to intercalate K in carbon based materials. With respect to the most stable intercalation sites at low AM concentrations, it can be concluded that the exact position and insertion energy depend on an interplay

between defect concentration, interlayer interaction and AM type.

Finally, it has to be noticed that putting the intercalant in the vicinity of a defect site typically results in changes of the C–C bond lengths in the neighbourhood. The observed changes depend on the size of the AM, such that the strongest curvature and the largest C–C bond change are observed for K intercalation.

### Charge/Discharge Profiles

After assessing the impact of defects on the intercalation strength with respect to single atoms, intercalation compounds with larger fractions of AMs have been investigated. For this purpose, the intercalation process of Li, Na and K in pristine graphite, and two defect-containing systems (MV and SW defect) have been studied. To understand the impact of the different defects on the whole intercalation process and the potential use as anode material the corresponding discharge curves have been determined for a series of  $AMC_x$  stoichiometries. The selected systems were filled with increasing AM contents and analyzed with respect to their respective stability. The intercalation sites for the additional AM atoms were chosen in a way to maximize the distance between AM atoms in one layer, starting in the vicinity of the most stable single atom sites determined above. After completely filling the first layer, corresponding to a  $AMC_{12-x}$  stoichiometry, the second layer was filled, considering different arrangements of the AM layers with respect to each other. For the phases that were found to be most stable at a given AM concentration, the open circuit voltages (OCV) with respect to the pure metal anodes have been determined via the following equation:<sup>[62]</sup>

$$V_{OCV} = E_{x+1} - (E_x + E_{AM})/z, \quad (3)$$

where  $x$  is the AM content and  $z$  corresponds to the elementary charges that are transferred during the intercalation process. The obtained voltages for the defect-free system as well as for MV and SW defects for Li, Na and K intercalation are depicted in Figure 4. While the voltage for Li and K remains positive in the

presence of the defect for all considered stoichiometries, it becomes negative for Na at higher stoichiometry, indicating that the system has become unstable, i.e. meaning that the intercalation limit is reached. However, unlike in a defect-free system, where Na intercalation is unfavorable already for tiny amounts of Na, in the defective system it becomes at least stable for low AM concentrations.

With respect to the intercalation process, it has to be noted that the interlayer spacing is strongly changed when different AMs are intercalated. This is best seen when comparing (hypothetical) defect-free  $KC_6$ ,  $NaC_6$ , and  $LiC_6$  model structures. The layer spacing for  $KC_6$  amounts to  $\approx 5.06 \text{ \AA}$  which is about 13% larger than for the case of Na and even more than 38% larger as compared to the intercalation of Li. Due to the large differences in ionic radii ( $Li^+$  (0.76  $\text{Å}$ )  $<$   $Na^+$  (1.02  $\text{Å}$ )  $<$   $K^+$  (1.38  $\text{Å}$ )), the increased volume for Na and K intercalation compounds is, however, not surprising.<sup>[63]</sup> As already discussed, for the defect-free system at AM contents close to  $AMC_{48}$  stoichiometry a change from AB to AA stacked layers is becoming more favorable. Note that in the following discussion the denoted stoichiometries in case of the MV defect neglect the removed carbon atom. For the MV defect, the AB layer stacking is observed to be favorable up to an  $AMC_{24}$  stoichiometry. For AM concentrations corresponding to  $LiC_{12}$  and  $NaC_{12}$  an AA layer stacking is observed, while for the case of  $KC_{12}$  a configuration with intermediate stacking (between AA and AB stacking) is found to be the most stable arrangement. Finally, for the case of  $AMC_6$  Li and Na remain AA stacked and also the K-intercalation compounds are approaching this ordering. The situation is similar for the SW defect. As the AM concentration increases to  $AMC_{24}$ , the AB stacking shifts towards an AA stacking, adapting intermediate configurations. However, when the AM concentration rises to  $AMC_{12}$  and higher, the AA stacking becomes more favorable for all AM intercalation compounds, while the exact concentration at which the transition takes place is expected to be AM specific. In comparison to the case of a MV defect, the transition to an AA stacking starts earlier in the case of the SW defect. This can be understood with the SW defect system being structurally closer to pristine defect-free graphite, where the transition was already found close to  $AMC_{48}$ .

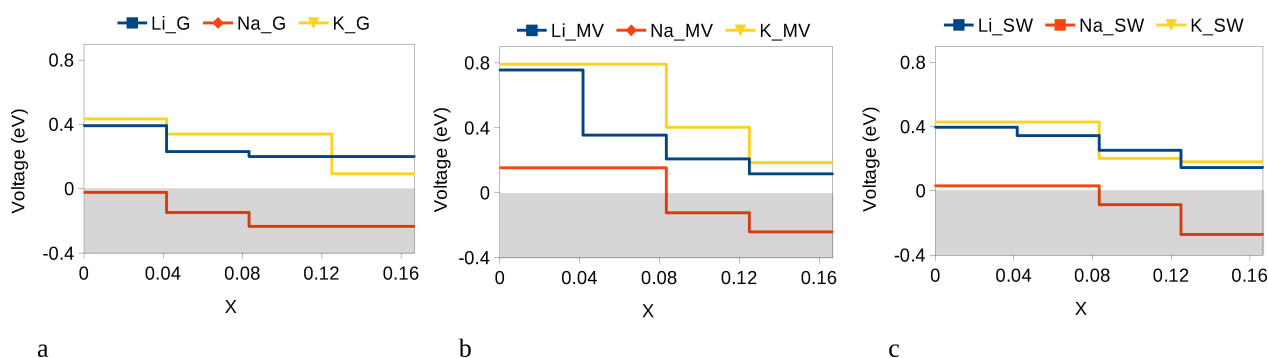


**Figure 4.** Charge/Discharge curves for Li, Na and K intercalation with respect to a) defect free graphite (G), as well as for model systems containing b) MV and c) SW defects calculated in the two-layer  $C_{144-x}$  model systems.  $X$  denotes the concentration of intercalated AMs in the investigated model systems ( $X$  corresponds to the number of intercalated AM atoms divided by the total number of atoms). The shaded area illustrates that in this part intercalation is energetically unfavorable.

Thus, as already expected from the single atom intercalation, defects enable the intercalation of larger fractions of AMs. However, this comes also along with higher intercalation voltages as can best be seen when comparing the MV and graphite systems. While defects thus result in additional capacity in the graphitic layers it also becomes clear that a large part of the AMs that are stored at low potential in hard carbon are not intercalated in the layers but fill micro and nanopores, in agreement with the current picture of AM insertion in hard carbon.<sup>[31,32,62]</sup> On the other hand it has to be pointed out that the intercalation increases the layer spacing and thus allows for better diffusion through the structure. Therefore, while the additional capacity may partially be due to strongly bound AMs that are responsible for the typically observed irreversible capacity loss during the first charge, the increased number of intercalated AM atoms can still be expected to positively affect the kinetics of the material.

### Phonon Dispersion Curves – the G-Band Shift

Raman scattering is a frequently used tool for characterizing graphitic structures, yielding a prominent peak at a frequency of  $\approx 1580\text{ cm}^{-1}$ , typically referred to as G-band. This peak corresponds to the creation/annihilation of an optical phonon with zero wave vector. Recent works have shown that the alkali metal intercalation in graphitic systems results in a frequency shift of this G-band to lower frequencies.<sup>[31,32]</sup> Before investigating the impact of the intercalation process, the effect of structural changes in the AM-free system has been studied. For this purpose the dispersion curves of pristine and curved graphite as well as for the case of MV and SW defects have been determined and were backfolded on the high-symmetry directions of graphite – following the reciprocal space direction  $\Gamma - K - M - \Gamma$  (see Figure 5). From a qualitative point of view, the dispersion curves of these four system do not show significant differences, thus pointing to a rather small impact of these structural modifications. This interpretation is confirmed when the G-band positions are extracted. Indeed, here only small variations with a maximum difference of  $15\text{ cm}^{-1}$  are observed (see Figure 5). Nevertheless, this indicates that increased defect concentrations are expected to result in a slightly increased G-band shift.

As a next step, the vibrational properties of MV and SW defect have been investigated with respect to different AM

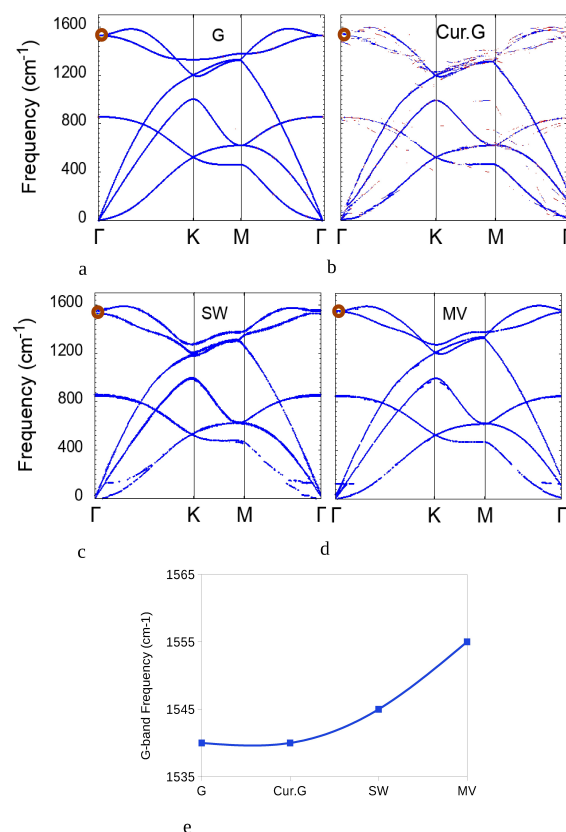


**Figure 5.** Back-folded phonon dispersion curves for a) pristine graphite (G), b) Curved graphite (Cur.G), c) Stone-Wales defect (SW) d) mono-vacancy (MV). Red circles, represent the predicted positions of phonons that contribute to the G-band. In (e) the G-band shift extracted from a)-d) is depicted.

contents. For this purpose the dispersion curves have again been backfolded on the high-symmetry direction  $\Gamma - K - M - \Gamma$  as depicted in Figure 6 (see also Figure S1 and Figure S2 in the SI). In addition, the G-band position for the two defect-containing systems has been extracted and compared to the defect-free case. Indeed, for both defect types, as well as for the defect-free system, the phonon dispersion curves show a clear red shift of the G-band for AM intercalation. This means that while defects affect the structure locally, the characteristics of the inplane carbon-carbon bonds, as probed by Raman scattering, are only slightly affected. Furthermore, for low intercalation contents Li, Na and K exhibit only slight differ-

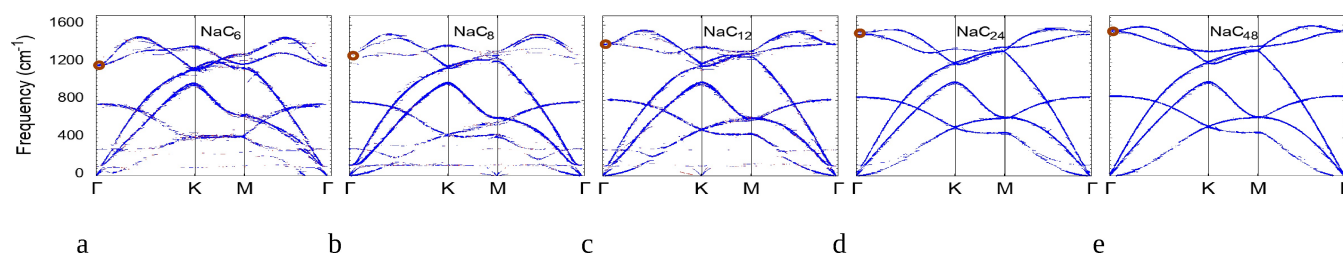


**Figure 6.** Back-folded phonon dispersion curves for Na intercalation for the MV defect structure as determined by DFT. Red circles, represent the predicted positions of phonons that contribute to the G-band.



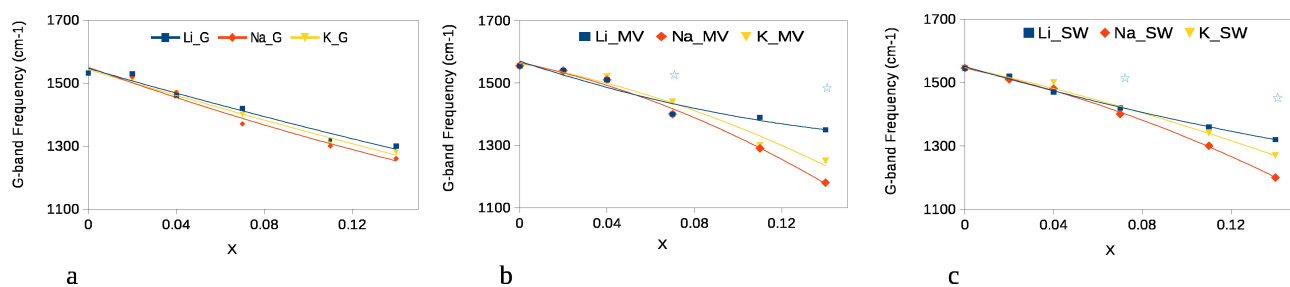


**Figure 7.** G-band shift for Li, Na and K intercalation, regarding a) defect free graphite (G), b) MV and c) SW defects, with X the AM concentration in the  $C_{144-x}$  model system (X corresponds to the number of AM atoms divided by the total number of atoms). Note that, the points marked with a star are computed for the  $C_{108-x}$  system and therefore correspond to a slightly higher defect concentration.

ences in G-band position for all scenarios (see Figure 6 as well as Figure S1 and Figure S2 in the SI). However, by increasing the intercalation content, differences between the AM types are observed, resulting in the strongest G-band shift for Na and the weakest for Li at high AM concentration (see Figure 7). This trend is observed for MV and SW defect as well as for the defect-free system. Surprisingly, the observed order does not directly correlate with the AM ionic radii and the corresponding lattice spacing. In fact, the G-band vibrations correspond to the inplane motion of the carbon atoms with the alkali metal atoms not participating in these motions. The different ion sizes and corresponding lattice spacings as well as their electronic structure result in differences in the charge transfer between the alkali metal species and the graphitic planes. The changing bonding situation in turn is responsible for a weakening of the in-plane force constants, thus causing the G-band shift, which consequently increases with the AM content.

On a qualitative level, the amount of intercalated alkali metal atoms is found to correlate with a decrease of the G-band frequency. In fact, the absolute G-band shift may even be utilized to determine the total number of intercalated AM atoms, with distinct intercalation limits and G-band minima for Li, Na, and K, thus offering a simple and effective way to quantify the degree of intercalation.

### Electronic Structure – the D-Band

Apart from the just discussed G-band there is an additional and rather unique feature in the Raman spectra of graphitic materials, the D-band. This Raman peak is, however, not a  $\Gamma$ -point phonon but is caused by a so-called double resonance Raman (DRR) process.<sup>[32]</sup> The availability of empty states in the band structure, particularly in the vicinity of the high symmetry points  $K$  and  $K'$ , is a requirement for the occurrence of a DRR process and, consequently, the D-band. In such a process, an excited electron, a non- $\Gamma$ -point phonon, and a structural defect are involved. First, the wave length of the Raman laser needs to be able to excite an electron to an empty state in the conduction band (see Figure 8). Before being backscattered by a lattice defect, the excited electron interacts with the crystal lattice resulting in the creation (annihilation) of a phonon. The electron then recombines with the hole it created in the

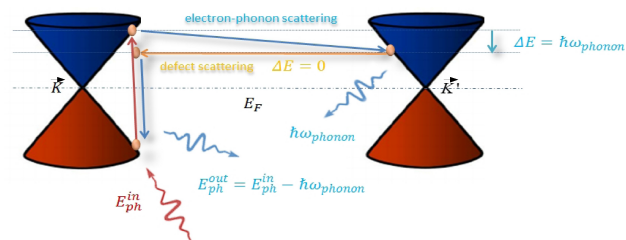


**Figure 8.** A double resonance process is illustrated schematically with respect to the electronic band structure near the highsymmetry points.

valence band and releases a photon with a longer (shorter) wavelength as a result of energy transfer to (from) the created (annihilated) phonon. It has to be noted that the graphite band structure displays the well-known Dirac cones at the high symmetry points of the Brillouin zone (at  $K$  and  $K'$ ), thus enabling the occurrence of the DRR process. In conclusion, DRR processes allow probing phonons distant from the center of the Brillouin zone, whereas first order Raman scattering is a technique for the research of phonons close to the G-point. As a result, DRR events provide insight beyond what is accessible by conventional Raman processes, even allowing to extract information on the electronic band structure.

To investigate correlations between AM intercalation and D-band occurrence, the electronic band structure was determined and also back-folded on the high-symmetry directions of the first Brillouin zone of graphite. This allows an analysis of our model compounds in a comparative manner. The obtained band structures nicely show the effect of alkali metal intercalation in pristine graphite and for both defect types, as depicted for the case of Na in Figure 9 (for Li and K see Figure S3 and Figure S4 in the SI).

As can be inferred from the band structure, the alkali metal atoms contribute their valence electrons to the system, essentially filling free states of the graphitic band structure (corresponding to a rigid band model like picture). The filling of these states then causes an upshift of the Fermi level. Thus, when the amount of alkali metals increases, the Fermi level continuously shifts upwards, which leads to a lack of free states in the conduction band, thus finally hindering the occurrence of a double resonance, corresponding to the experimentally observed disappearing D-band.<sup>[31,32]</sup> This is indicated by the red arrows in Figure 9 (see also Figure S3 and Figure S4 in the SI),

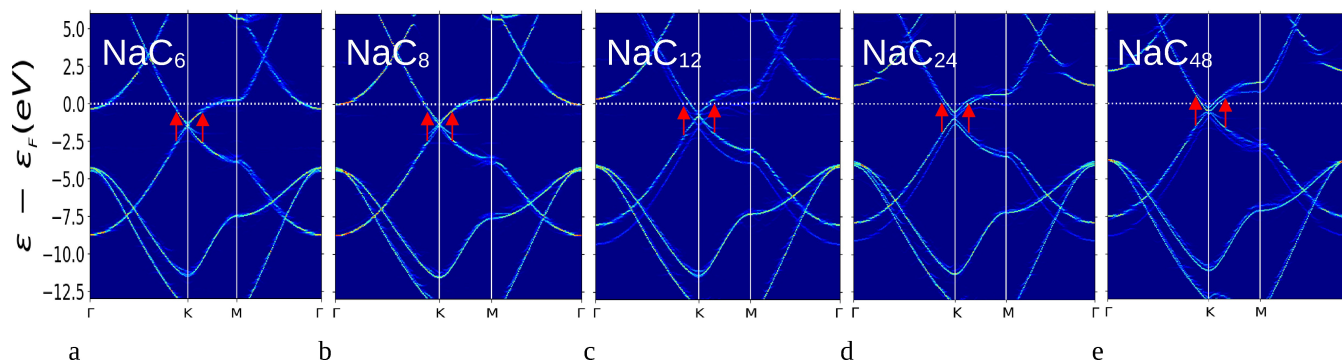


**Figure 9.** Electronic band structure of MV defect back-folded to the Brillouin zone of graphite for Na intercalation regarding different stoichiometry. The red arrows in the vicinity of the K-point in reciprocal space, corresponding to the typical excitation energy of a laser applied in Raman experiments, having a wavelength of 633 nm (1.96 eV).

which show the states in the vicinity of the K-point that could be reached by a typical Raman laser of wavelength 633 nm. Note that the length of the arrow corresponds to the energy of such a laser. The analysis of the back-folded band structures reveals that for sodium and potassium compounds with AM contents beyond  $\text{AMC}_{12}$  no states are accessible above the Fermi energy, whereas the lithium compounds still offer free states beyond that concentration. This indicates that while DRR processes are no longer permitted for Na and K, they are still possible for Li. Hence, the D-band is expected to disappear for lower AM concentrations in the case of Na and K. This trend is similar for the MV and the SW defect as well as for the defect-free system, with the Fermi level shifting a bit slower for the MV case, which is due to the filling of missing electrons in the defect site. The overall rather small differences, however, indicate that the band structure is only slightly affected by the presence of defects. Observable changes with respect to the AM type on the other hand again emphasize differences in the charge transfer. To better quantify the differences in the band structure, the shift in Fermi level as a function of the number of intercalated AM atoms was extracted and depicted in Figure 10. For all three cases (pristine, MV and SW) the graphs show two distinct regimes for the Fermi level shift. First there is an almost perfectly linear shift of the Fermi level with respect to the number of intercalated AM atoms. This behaviour is observed as long as the intercalation corresponds to the filling of one

layer, with the other one remaining empty. This indeed corresponds to a rigid-band like model with the band structure being gradually filled by the additional electrons. Interestingly, the different slopes for Li, Na and K also point to differences in the charge transfer mechanism. Due to their larger size and the therefore increased layer spacing, K and Na show a similar charge transfer, while the small Li atom behaves differently. With respect to the energetic stability on the other hand Li and K show, at first glance, more similarities. This is however caused by the exceptional behaviour of Li, which shows covalent components in its bonds to the neighbouring C atoms.<sup>[64]</sup> When the AM content increases and the second layer is filled the band structure is, in particular for Na and K intercalation, more significantly changed, thus not fulfilling the same linear scaling any more.

In fact, for all Li contents, we detect degenerate bands for the Dirac cone at the K-point, whereas for Na and K intercalation, except for high contents, a splitting is shown. This splitting is a consequence of the increased ion size of Na and K, which results in different layer spacings between empty and AM-containing layers. This can nicely be shown by investigating AM-free structures that show different layer spacings e.g. corresponding to those of a  $\text{KC}_{12}$  intercalation compound (see Figure 5 in the SI). In principle, this splitting is a consequence of a lowering in symmetry. This also explains why it is observed

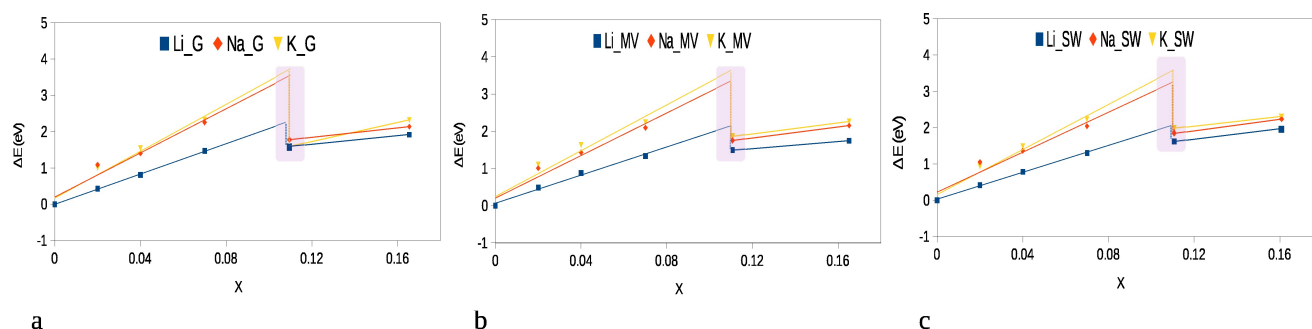


**Figure 10.** Fermi-energy shift for different stoichiometry regarding a) pristine graphite, b) MV, and c) SW defects, (X corresponds to the number of AM atoms divided by the total number of atoms).

for AB stacked graphite but not for its AA stacked analogon (see Figure S6 in the SI).

When comparing the band structure of the pristine and low AM-content samples for the considered defect types and concentrations, there are only small changes (see e.g. Figure S3 and S4 in the SI) visible. Increasing defect concentrations on the other hand may have a more significant impact on the appearance of the band structure (*i.e.* on the band shape), while higher AM contents essentially result in the above discussed filling of states (rigid band model) and thus a shifting Fermi level.

To summarize, the electronic band structure of the graphitic domains is not largely altered by the presence of defects. The experimentally observed disappearance of the D-band during AM intercalation and its association with a shifting Fermi level is found to be valid for all investigated cases, thus further corroborating the extended card house model.<sup>[31,32]</sup> Furthermore, the point at which the D-band disappears during the AM intercalation, can in addition be used to determine a lower boundary of the intercalation limit of HC electrodes.

## Conclusions

In conclusion, we used first-principles calculations to investigate the intercalation of Li, Na, and K in defect-containing, graphite based model systems to mimic the intercalation process in hard carbon anodes. According to our results, the presence of defects promotes the stability of AM intercalation, in particular when unsaturated carbon bonds are present. Thus, defects in principle can increase the capacity of interlayer storage in carbon based materials. However, parts of this additional capacity, in particular alkali metal atoms at the defect centers, may be responsible for the experimentally observed irreversible capacity losses during the first charge. On the other hand, additional interlayer sites are also created at low potentials and these, together with an increased layer spacing, are important for allowing a fast diffusion of AMs to micro- and nano-pores. These insights might be used for the rational design of hard carbon based anode materials with improved properties.

Finally, we demonstrated that the intercalation process in pristine and defective graphite results in a similar change in the vibrational spectrum, most prominently in the shift of the G-band vibrations towards lower frequencies. Thus, in agreement with earlier studies, a shifting G-band can clearly be linked to the intercalation process in the graphitic domains, whereas a constant G-band position during discharge/charge means alkali metal adsorption/desorption in micro- and nano-pores of hard carbon anodes. Finally, the occurrence of the D-band with respect to the alkali metal content has been discussed, showing that defect concentrations in the order of almost 1% do not significantly alter the band structure. This also means that the D-band, or to be precise its disappearance, yields additional information on the intercalation process in the graphitic domains of HC. Hence, the experimentally observed G-band shift and the disappearing D-band clearly corroborate the

extended card house model for AM intercalation in hard carbon.<sup>[31,32]</sup>

## Acknowledgements

This work was funded by the Deutsche Forschungsgemeinschaft (DFG, German Research Foundation) under Project ID 390874152 (POLiS Cluster of Excellence, EXC 2154). The authors acknowledge further support by the state of Baden-Württemberg through bwHPC and the German Research Foundation (DFG) through grant no INST 40/575-1 FUGG (JUSTUS 2 cluster) and by the HoreKa supercomputer funded by the Ministry of Science, Research and the Arts Baden-Württemberg and by the Federal Ministry of Education and Research. This work contributes to the research performed at CELEST (Center for Electrochemical Energy Storage Ulm-Karlsruhe). HE gratefully acknowledges funding from the German Bundesministerium für Bildung und Forschung (BMBF), project "NETPEC" (No. 01LS2103A). Open Access funding enabled and organized by Projekt DEAL.

## Conflict of Interests

There are no conflicts to declare.

## Data Availability Statement

The data that support the findings of this study are available from the corresponding author upon reasonable request.

**Keywords:** Post-Li-ion batteries · Hard-carbon · Defect · Phonon dispersion · Fermi-energy

- [1] M. Broussely, From Lithium to Lithium Ion, a 40 Year Battery Generation (Battery Technology Award Address), in *ECS Meeting Abstracts*, 10, IOP Publishing 2007 page 663.
- [2] L. He, W. Xu, Y. Song, Y. Luo, X. Liu, Z. Zhao, *Global Challenges* 2018, 2, 1700079.
- [3] M. Rahimi, Lithium-ion batteries: Latest advances and prospects 2021.
- [4] Y. Yue, H. Liang, *Small Methods* 2018, 2, 1800056.
- [5] C. Gauckler, M. Dillenz, F. Maroni, L. F. Pfeiffer, J. Biskupek, M. Sotoudeh, Q. Fu, U. Kaiser, S. Dsoke, H. Euchner, P. Axmann, M. Wohlfahrt-Mehrens, A. Groß, M. Marinaro, *ACS Appl. Energ. Mater.* 2022, 5, 13735.
- [6] H. Onuma, K. Kubota, S. Muratubaki, W. Ota, M. Shishkin, H. Sato, K. Yamashita, S. Yasuno, S. Komaba, *J. Mater. Chem. A* 2021, 9, 11187.
- [7] A. V. Desai, R. E. Morris, A. R. Armstrong, *ChemSusChem* 2020, 13, 4866.
- [8] D. Stottmeister, A. Groß, *Batteries & Supercaps* 2023, 6, e202300156.
- [9] O. Lenchuk, P. Adelhelm, D. Mollenhauer, *Phys. Chem. Chem. Phys.* 2019, 21, 19378.
- [10] J. Zhang, Y. Li, L. Zhu, X. Wang, J. Tu, *Energy Storage Mater.* 2021, 41, 606.
- [11] J. Xu, Y. Dou, Z. Wei, J. Ma, Y. Deng, Y. Li, H. Liu, S. Dou, *Adv. Sci.* 2017, 4, 1700146.
- [12] T. Yamamoto, A. Yadav, T. Nohira, *J. Electrochem. Soc.* 2022, 169, 050507.
- [13] L. Li, L. Liu, Z. Hu, Y. Lu, Q. Liu, S. Jin, Q. Zhang, S. Zhao, S.-L. Chou, *Angew. Chem. Int. Ed.* 2020, 59, 12917.
- [14] Z. Jian, W. Luo, Z. Xing, C. Bommier, Z. Li, X. Ji, Carbon Electrodes for Potassium-Ion Batteries, in *Electrochemical Society Meeting Abstracts imlb2016*, 2, The Electrochemical Society, Inc. 2016 pages 821–821.
- [15] J. Zhao, X. Zou, Y. Zhu, Y. Xu, C. Wang, *Adv. Funct. Mater.* 2016, 26, 8103.

- [16] Y. Liu, B. V. Merinov, W. A. Goddard III, *Proc. Natl. Acad. Sci. USA* **2016**, *113*, 3735.
- [17] M. Khosravi, N. Bashirpour, F. Nematpour, *Adv. Mater. Res.* **2014**, *829*, 922.
- [18] X. Zhang, S. Han, P. Xiao, C. Fan, W. Zhang, *Carbon* **2016**, *100*, 600.
- [19] S. M. Jafari, M. Khosravi, M. Mollazadeh, *Electrochim. Acta* **2016**, *203*, 9.
- [20] H. Yu, X. Dong, Y. Pang, Y. Wang, Y. Xia, *Electrochim. Acta* **2017**, *228*, 251.
- [21] I. Saldos, *Nanotechnology, Science and Applications* **2010**, pages 101–106.
- [22] H. Zheng, Q. Qu, L. Zhang, G. Liu, V. S. Battaglia, *RSC Adv.* **2012**, *2*, 4904.
- [23] M. Drews, J. Büttner, M. Bauer, J. Ahmed, R. Sahu, C. Scheu, S. Vierrath, A. Fischer, D. Biro, *ChemElectroChem* **2021**, *8*, 4750.
- [24] M. Thompson, Q. Xia, Z. Hu, X. S. Zhao, *Materials Advances* **2021**, *2*, 5881.
- [25] A. Kamiyama, K. Kubota, T. Nakano, S. Fujimura, S. Shiraishi, H. Tsukada, S. Komaba, *ACS Appl. Energ. Mater.* **2019**, *3*, 135.
- [26] H. Yamamoto, S. Muratsubaki, K. Kubota, M. Fukunishi, H. Watanabe, J. Kim, S. Komaba, *J. Mater. Chem. A* **2018**, *6*, 16844.
- [27] Z. Jian, Z. Xing, C. Bommier, Z. Li, X. Ji, *Adv. Energy Mater.* **2016**, *6*, 1501874.
- [28] A. Kamiyama, K. Kubota, T. Nakano, S. Fujimura, S. Shiraishi, H. Tsukada, S. Komaba, *ACS Appl. Energ. Mater.* **2019**, *3*, 135.
- [29] E. Buiel, A. George, J. Dahn, *Carbon* **1999**, *37*, 1399.
- [30] J. Dahn, W. Xing, Y. Gao, *Carbon* **1997**, *35*, 825.
- [31] M. Anji Reddy, M. Helen, A. Groß, M. Fichtner, H. Euchner, *ACS Energy Lett.* **2018**, *3*, 2851.
- [32] H. Euchner, B. P. Vinayan, M. A. Reddy, M. Fichtner, A. Groß, *J. Mater. Chem. A* **2020**, *8*, 14205.
- [33] K. Kubota, S. Shimadzu, N. Yabuuchi, S. Tominaka, S. Shiraishi, M. Abreu-Sepulveda, A. Manivannan, K. Gotoh, M. Fukunishi, M. Dahbi, et al., *Chem. Mater.* **2020**, *32*, 2961.
- [34] H. Jang, I. Hasa, H. Kim, Y. Hwa, Y.-W. Byeon, R. Kostecki, H. Kim, *J. Electrochem. Soc.* **2023**, *170*, 090538.
- [35] H. Alptekin, H. Au, A. C. Jensen, E. Olsson, M. Goktas, T. F. Headen, P. Adelhelm, Q. Cai, A. J. Drew, M.-M. Titirici, *ACS Appl. Energ. Mater.* **2020**, *3*, 9918.
- [36] Nagmani, S. Puravankara, *ACS Appl. Energ. Mater.* **2020**, *3*, 10045.
- [37] B. Xiao, T. Rojo, X. Li, *ChemSusChem* **2019**, *12*, 133.
- [38] V. Simone, A. Boulineau, A. De Geyer, D. Rouchon, L. Simonin, S. Martinet, *J. Energy Chem.* **2016**, *25*, 761.
- [39] D. Ledwoch, D. J. Brett, E. Kendrick, *ECS Trans.* **2016**, *72*, 17.
- [40] A. Baranov, Y. S. Bobovich, V. Petrov, *J. Raman Spectrosc.* **1993**, *24*, 695.
- [41] C. Thomsen, S. Reich, *Phys. Rev. Lett.* **2000**, *85*, 5214.
- [42] T. Dines, D. Tither, A. Dehbi, A. Matthews, *Carbon* **1991**, *29*, 225.
- [43] H. Jalili, B. Aslibeiki, A. Hajalilou, O. Musalu, L. Ferreira, M. Cruz, *Ceram. Int.* **2022**, *48*, 4886.
- [44] M. Drews, J. Büttner, M. Bauer, J. Ahmed, R. Sahu, C. Scheu, S. Vierrath, A. Fischer, D. Biro, *ChemElectroChem* **2021**, *8*, 4750.
- [45] Z. Li, C. Bommier, Z. Chong, Z. Jian, T. Surta, X. Wang, Z. Xing, J. Neufeind, W. Stickle, M. Dolgos, et al., *Adv. Energy Chem.* **2017**, *7*, 1602894.
- [46] A. Vasileiadis, Y. Li, Y. Lu, Y.-S. Hu, M. Wagemaker, *ACS Appl. Energ. Mater.* **2022**, *6*, 127.
- [47] Z. Zhao, H. Chen, W. Zhang, S. Yi, H. Chen, Z. Su, B. Niu, Y. Zhang, D. Long, *Materials Advances* **2023**.
- [48] J. Meng, G. Jia, H. Yang, M. Wang, *Front. Chem.* **2022**, *10*, 986541.
- [49] G. Kresse, J. Furthmüller, *Phys. Rev. B* **1996**, *54*, 11169.
- [50] G. Kresse, D. Joubert, *Phys. Rev. B* **1999**, *59*, 1758.
- [51] G. Kresse, J. Furthmüller, *Comput. Mater. Sci.* **1996**, *6*, 15.
- [52] P.-c. Tsai, S.-C. Chung, S.-k. Lin, A. Yamada, *J. Mater. Chem. A* **2015**, *3*, 9763.
- [53] A. Togo, I. Tanaka, *Scr. Mater.* **2015**, *108*, 1.
- [54] P. V. Medeiros, S. Stafström, J. Björk, *Phys. Rev. B* **2014**, *89*, 041407.
- [55] P. V. Medeiros, S. S. Tsirkin, S. Stafström, J. Björk, *Phys. Rev. B* **2015**, *91*, 041116.
- [56] F. Zheng, P. Zhang, *Comput. Phys. Commun.* **2017**, *210*, 139.
- [57] L. Li, S. Reich, J. Robertson, *Phys. Rev. B* **2005**, *72*, 184109.
- [58] I. A. Pašti, A. Jovanović, A. S. Dobrota, S. V. Mentus, B. Johansson, N. V. Skorodumova, *Phys. Chem. Chem. Phys.* **2018**, *20*, 858.
- [59] M. Heggie, G. Haffenden, C. Latham, T. Trevethan, *Philos. Trans. R. Soc. London Ser. A* **2016**, *374*, 20150317.
- [60] F. L. Thiemann, P. Rowe, A. Zen, E. A. Muller, A. Michaelides, *Nano Lett.* **2021**, *21*, 8143.
- [61] C. Tayran, S. Aydin, M. Cakmak, Ş. Ellialtıoğlu, *Solid State Commun.* **2016**, *231*, 57.
- [62] H. Euchner, A. Groß, *Phys. Rev. Mater.* **2022**, *6*, 040302.
- [63] N. Yoshinari, T. Konno, *Chem. Lett.* **2021**, *50*, 697.
- [64] H. Moriwake, A. Kuwabara, C. A. Fisher, Y. Ikuhara, *RSC Adv.* **2017**, *7*, 36550.

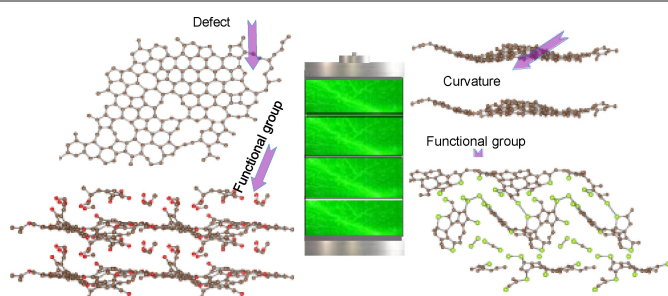
Manuscript received: October 16, 2023

Revised manuscript received: February 20, 2024

Accepted manuscript online: February 27, 2024

Version of record online: ■■■, ■■■





HC is a promising material for post-lithium-ion batteries. Considering the variety of defects, functional groups,

curvature, and porosity HC shows unique properties compared to commonly used graphite.

*J. Azizi, A. Groß, H. Euchner\**

1 – 13

## Computational Investigation of Carbon Based Anode Materials for Li- and Post-Li- Ion Batteries

